



# Flexible and freestanding core-shell SnO<sub>x</sub>/carbon nanofiber mats for high-performance supercapacitors



Edmund Samuel <sup>a,1</sup>, Bhavana Joshi <sup>a,1</sup>, Hong Seok Jo <sup>a</sup>, Yong Il Kim <sup>a</sup>, Mark T. Swihart <sup>b</sup>, Je Moon Yun <sup>c</sup>, Kwang Ho Kim <sup>c,d,\*\*</sup>, Sam S. Yoon <sup>a,\*</sup>

<sup>a</sup> School of Mechanical Engineering, Korea University, Seoul 02841, Republic of Korea

<sup>b</sup> Department of Chemical & Biological Engineering, University at Buffalo, The State University of New York, Buffalo, NY 14260–4200, USA

<sup>c</sup> Global Frontier R&D Center for Hybrid Interface Materials, Pusan National University, San 30 Jangjeon-dong, Geumjeong-gu, Busan 609-735, Republic of Korea

<sup>d</sup> School of Materials Science and Engineering, Pusan National University, San 30 Jangjeon-dong, Geumjeong-gu, Busan 609-735, Republic of Korea

## ARTICLE INFO

### Article history:

Received 5 March 2017

Received in revised form

2 August 2017

Accepted 9 September 2017

Available online 12 September 2017

### Keywords:

Electrospinning

SnO<sub>x</sub>/CNF core-shell

Flexible

Supercapacitor

## ABSTRACT

We demonstrate the fabrication of core-shell SnO<sub>x</sub>/carbon nanofiber (CNF) composite mats via single-nozzle one-step electrospinning for use as flexible freestanding electrodes in supercapacitors. The freestanding and flexible nature of the composites is essential for their use in lightweight, portable, and foldable electronic devices and eliminates the need for a separate current collector. We fully characterized the structural and morphological properties of the SnO<sub>x</sub>/CNF mats and optimized the SnO<sub>x</sub> to CNF precursor ratio. The optimized SnO<sub>x</sub>/CNF-based symmetric supercapacitor exhibited a capacitance of 289 F·g<sup>-1</sup> at a scan rate of 10 mV·s<sup>-1</sup>. Moreover, it retained more than 88% of its initial capacitance after 5000 cycles, highlighting the long-term stability of supercapacitors based on these SnO<sub>x</sub>/CNF mats.

© 2017 Elsevier B.V. All rights reserved.

## 1. Introduction

Electrochemical energy storage devices are primarily of three types: (1) rechargeable batteries; (2) electrochemical capacitors, conventionally known as supercapacitors; and (3) supercapatteries (hybrids of batteries and supercapacitors) [1]. Among these, supercapacitors can be of great utility in portable electronics and automotive applications owing to their high power density, short charge/discharge time, and long cycling life [2,3]. Supercapacitors based on carbon materials such as graphene, carbon nanofibers (CNFs), activated carbon, and carbon nanotubes are known as electrical double layer capacitors (EDLCs). These EDLCs store energy through the electrostatic adsorption of ions on the electrode surface alone [1,4]. The electrostatic adsorption of ions occurs at the

electrolyte/electrode interface in the absence of chemical reactions [5]. However, because the process is a physical one (involving only the adsorption of ions and no chemical reaction), EDLCs exhibit relatively low energy densities. Supercapacitors that employ electroadsorption or redox reactions on the surface of the electrodes are called pseudocapacitors. The redox reactions that occur in these pseudocapacitors are reversible and involve multi-electron Faradaic charge transfer, resulting in higher specific capacitances and energy densities than can be achieved in EDLCs [6]. Use of metal oxides in pseudocapacitors allows exploitation of multi-electron Faradaic processes to achieve high specific charge storage capacity.

Metal oxides such as RuO<sub>2</sub> [7], V<sub>2</sub>O<sub>5</sub> [8], MnO<sub>2</sub> [9,10], SnO<sub>x</sub> [11–13] and TiO<sub>2</sub> [14] have been investigated extensively for use in pseudocapacitors, and electrodes based on these materials have been fabricated using various methods. Transition metal oxides can store energy directly because of their extremely high pseudocapacitance (they undergo fast surface redox reactions because of the electro-absorption and electro-desorption of ions with electron transfer) [15,16]. Of these metal oxides, SnO<sub>x</sub> is nontoxic and inexpensive and is a high-capacitance electrode material that can operate in a broad negative-to-positive potential window. In addition, SnO<sub>x</sub> has a low electron chemical potential, which results

\* Corresponding author.

\*\* Corresponding author. Global Frontier R&D Center for Hybrid Interface Materials, Pusan National University, San 30 Jangjeon-dong, Geumjeong-gu, Busan 609-735, Republic of Korea.

E-mail addresses: [kwhokim@pusan.ac.kr](mailto:kwhokim@pusan.ac.kr) (K.H. Kim), [skyoons@korea.ac.kr](mailto:skyoons@korea.ac.kr) (S.S. Yoon).

<sup>1</sup> These authors have contributed equally.

in fast redox reactions, making  $\text{SnO}_x$  ideal for use as a supercapacitor electrode material [17]. However, the applicability of  $\text{SnO}_x$  as an electrode material is limited because of its low electrical conductivity. On the other hand, while alternative supercapacitor materials such as carbonized polymers, graphene and CNT show higher electrical conductivities, they have a limited ability to store charge. Thus, supercapacitors based on these materials cannot match the high energy densities that can be achieved using metal oxides [6,18].

The high energy density of  $\text{SnO}_x$  and high electrical conductivity of carbon are important factors to consider when selecting synergistic active materials for the electrodes of supercapacitors. The combination of  $\text{SnO}_x$  and carbon materials can exhibit a synergistic effect, as demonstrated by earlier studies [19,20].

In general, nickel foil, a nickel foam, stainless steel, or carbon cloth has been used as a current collector to improve the overall electrode conductivity [21]. However, the inclusion of a current collector upon which the active electrode material is deposited increases the mass of the supercapacitor. In addition, the inclusion of graphene or/and CNT would increase the overall production cost. The use of CNF would eliminate the use of the current collector as well as the graphene/CNT because CNF itself serves as a collector and conductor. As a result, composites of  $\text{SnO}_x$  and electronically conductive CNFs produced via electrospinning are being explored for producing lightweight, flexible, and freestanding electrodes for supercapacitors [22]. In addition, composites of CNFs and  $\text{SnO}_x$  exhibit a synergistic effect, resulting in the shortening of the diffusion path for the ions from the electrolyte to the electrode as well as an increase in the interfacial electron redox chemistry. Joshi et al. fabricated a  $\text{SnO}_x$ /CNF composite and studied its increased conductivity as well as the buffering effect [23]. CNF composites show a higher capacitance owing to the capacitive mechanism of the very thin double layer and their high surface-to-volume ratio [24,25]. However,  $\text{SnO}_x$ /CNF composites exhibited low rate capability because the micropores of the CNFs restrict the diffusion of ions at high scan rates and high current-density charge/discharge rates [4]. The core-shell nanostructure considered here facilitates a reduction in the ion diffusion length through the carbon shell. Furthermore, the Faradaic reaction also improves by transporting electrons through a continuous fiber, rather than a particle-to-particle structure. As a result, electrochemical properties are enhanced [26,27].

Here, we demonstrate an aqueous electrolyte-based symmetric supercapacitor based upon  $\text{SnO}_x$ /CNF core-shell structured composites. However, our CNF composite has mixed phase of Sn ( $x = 0$ ),  $\text{SnO}$  ( $x = 1$ ) and  $\text{SnO}_2$  ( $x = 2$ ). Where,  $x$  reflects the oxidation state of Sn, ranging from zero (for  $x = 0$ ) to 4+ (for  $x = 2$ ). Poly(methyl methacrylate) (PMMA) was used as a sacrificial polymer, as it decomposes at high temperatures to generate void space in the CNFs. During carbonization, the PMMA was eliminated from the turbostratic CNFs and replaced by  $\text{SnO}_x$ , producing the core( $\text{SnO}_x$ )-shell(CNF) structure. Further, the fabricated composite materials contain mesopores that allow rapid ion transport and ion adsorption/desorption at the electrode/electrolyte interface [4]. The single-nozzle approach provides a remarkably simple route to these core-shell structures. We produced the core-shell structures in a one-step deposition, without added processing steps such as etching, the use of a slurry, or impregnation with another material. Only simple heating processes were required to remove the PMMA and carbonize the polyacrylonitrile (PAN) in the electrospun fibers to yield the core-shell composites. In addition, the freestanding nature of the composites and the fact that they are operated well without a metallic current collector increase the specific capacitance of the overall device. This work is the first example of the use of core ( $\text{SnO}_x$ )-shell (CNF) structures in a full supercapacitor.

## 2. Experimental

### 2.1. Fabrication of $\text{SnO}_x$ /CNF composite

Freestanding NF (nanofiber) mats were synthesized using tin(II) acetate ( $\text{SnAc}$ ,  $\text{Sn}(\text{CH}_3\text{CO}_2)_2$ ; Sigma-Aldrich) as the metal source and *N,N*-dimethylformamide (DMF; 99.8%; Sigma-Aldrich) as the solvent, while polyacrylonitrile (PAN;  $M_w = 150$  kDa; Sigma-Aldrich) was used as the electrospinning polymer and PMMA ( $M_w \approx 120,000$  kDa; Sigma-Aldrich) as the sacrificial polymer. First, 7.6 wt% PAN and 0.4 wt% PMMA were dissolved in DMF, and the mixture was stirred for 24 h at 60 °C. Then, SnAc was added to this PAN/PMMA–DMF solution in different proportions, and the resulting mixtures were stirred again for 24 h at room temperature to form homogeneous solutions. The total amounts of SnAc in the different polymer solutions were 0, 0.5, 2, 4, and 6 wt%; the CNF mats obtained using these solutions are labeled as SnO-0, SnO-1, SnO-2, SnO-3, and SnO-4, respectively. However, we primarily focused on samples SnO-1, SnO-2, and SnO-3, as sample SnO-4, which corresponded to a SnAc concentration of 6 wt% exhibited a capacitance lower than that of SnO-3. The setup used for electrospinning consisted of a syringe and a needle, a grounded collector, and a high-voltage supply, as shown in Fig. 1a. The PAN/PMMA/SnAc solutions were electrospun at room temperature on an aluminum collector placed 15 cm away from the needle. The precursor SnAc solution was delivered from a syringe pump at a flow rate that ensured a stable Taylor cone was formed at the end of the needle. The electrospun mats were stabilized by heat treatment in air at 280 °C; the temperature was ramped up from room temperature to 280 °C at a rate of 5 °C  $\text{min}^{-1}$ . Next, the stabilized mats were annealed in a tube furnace in a flow of Ar at 800 °C for 2 h. This annealing process, which involved heating from room temperature at a rate of 3 °C  $\text{min}^{-1}$ , was performed to carbonize the PAN NFs. This process yielded flexible and freestanding core-shell-structured black  $\text{SnO}_x$ /CNF mats, as shown in Fig. 1b. Electrospinning of PAN/PMMA generally results in a tubular shape with PMMA at the core [28,29], owing to the interfacial tension, viscosity, and elasticity of the PAN/PMMA mixture [28]. However, during the carbonization process, the PMMA was removed from the electrospun mats and replaced by  $\text{SnO}_x$ , generating the core-shell ( $\text{SnO}_x$ /CNF) structure.

### 2.2. Characterization

The carbonized freestanding mats were characterized to determine their structural, morphological, chemical, and electrochemical properties. X-ray diffraction (XRD, SmartLab, Rigaku) was used to study the crystalline structures of the mats. A Raman spectrometer (LabRam ARAMIS IR2, HORIBA JOBIN YVON system) was used to analyze the carbon content and amount of carbon defects in the mats. The chemical states of elements in the mats were measured by X-ray photoelectron spectroscopy (XPS, Theta Probe Base System, Thermo Fisher Scientific Co.). The surface morphologies and elemental composition and distribution of the fabricated mats were evaluated using a scanning electron microscope (SEM, S-5000, Hitachi, Ltd.) and a transmission electron microscope (TEM, JEM 2100F, JEOL Inc.).

### 2.3. Electrochemical tests

Next, symmetric supercapacitors were prepared using two  $\text{SnO}_x$ /CNF flexible electrodes of the same diameter (14 mm), which were assembled in a coin-type cell (CR2032). A microporous polyethylene film (Celgard 3501; Celgard, South Korea) was used as the separator between the two electrodes. The electrolyte used was 6 M KOH. All the electrochemical measurements were performed at

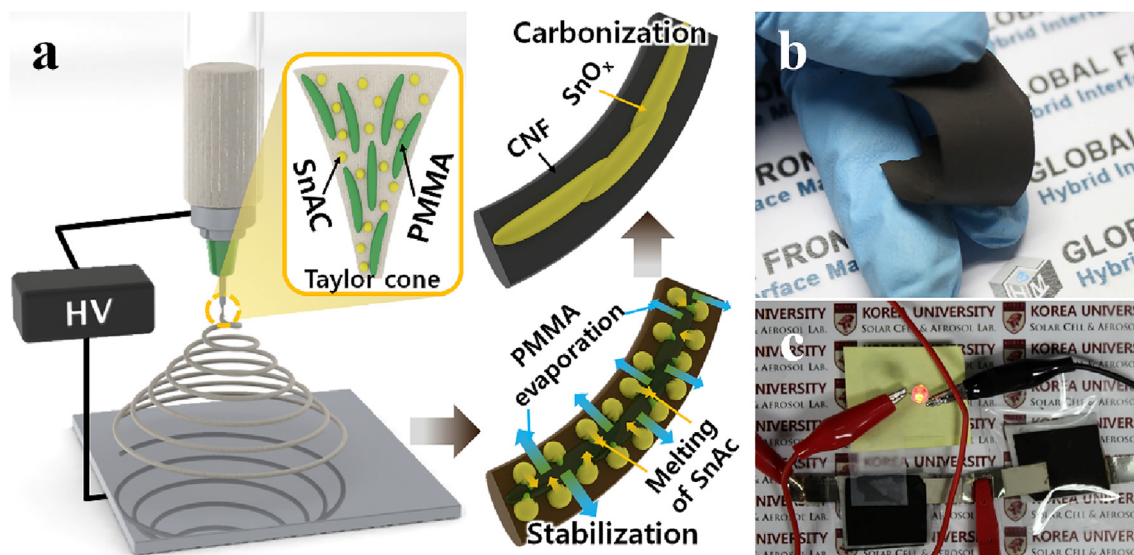


**Fig. 1.** (a) Schematic of process for fabricating  $\text{SnO}_x/\text{CNF}$  composites using electrospinning. (b) Photograph of flexible  $\text{SnO}_x/\text{CNF}$  composite. (c) LED test performed using two symmetric supercapacitors.

room temperature ( $25^\circ\text{C}$ ) using a WBCS300 battery cycling system (WonAtech, South Korea). Cyclic voltammetry (CV) measurements were performed on the various cells at different scan rates (2, 5, 10, 20, 30, 50, and  $100\text{ mV}\cdot\text{s}^{-1}$ ). In addition, galvanostatic charge/discharge cycling was also carried out at 0.1, 0.2, 0.5, 1, 2, 3 and  $5\text{ A}\cdot\text{g}^{-1}$ . Fig. 1c shows the setup used for a light-emitting diode (LED) glow test performed using supercapacitors based on composite sample SnO-3. For the LED test, two symmetric supercapacitors were arranged in series, with the dimensions of each supercapacitor being  $2.5 \times 2.5\text{ cm}^2$ . The high intensity of the LED when turned on indicated qualitatively that SnO-3 showed good energy and power densities.

### 3. Results and discussion

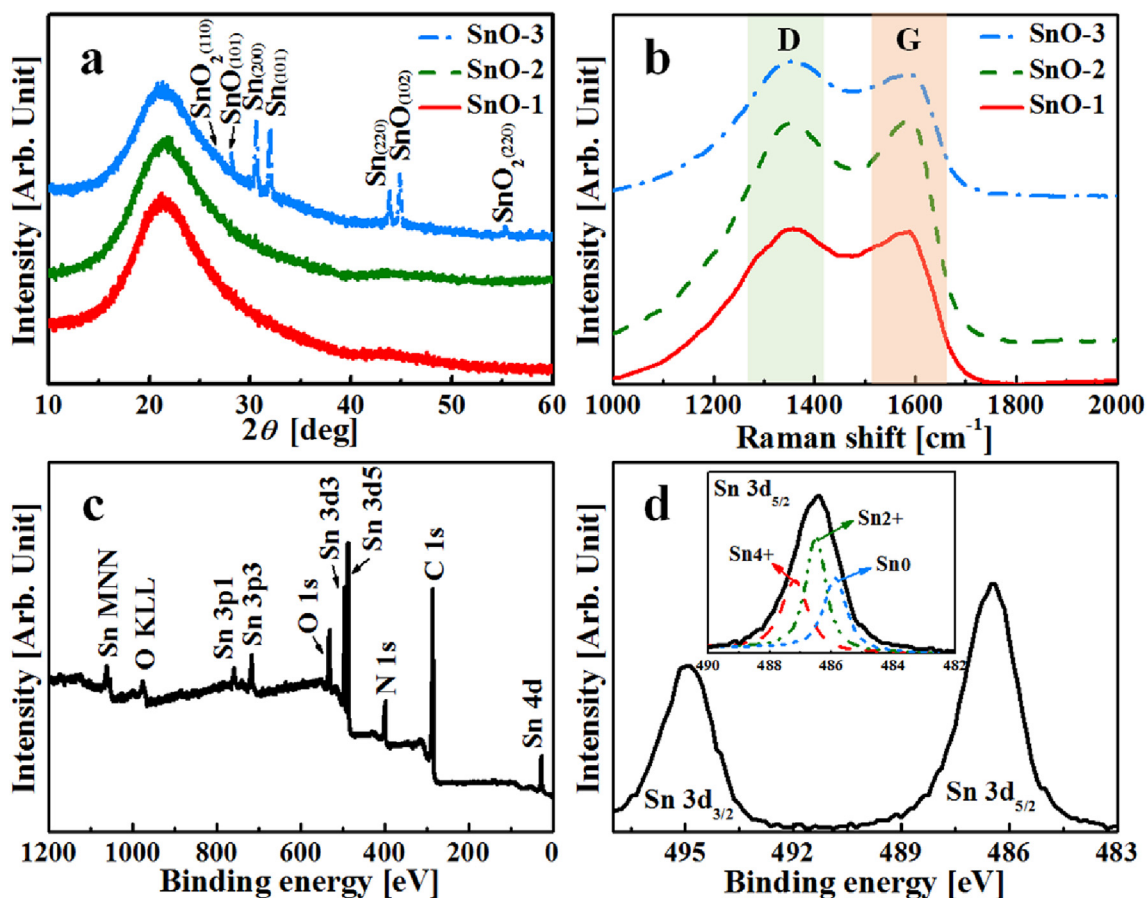
The X-ray diffraction patterns of the  $\text{SnO}_x/\text{CNF}$  composite mats obtained after annealing at  $800^\circ\text{C}$  are shown in Fig. 2a. Well-defined peaks can be seen only in the case of the sample corresponding to a SnAc concentration of 4 wt%, indicating that the crystallinity of  $\text{SnO}_x$  was high only at higher SnAc concentrations. Three different phases were present in the samples, as per an analysis of the diffraction patterns. The weak peaks at  $2\theta = 26.7^\circ$  and  $55^\circ$  correspond to the (110) and (220) planes of  $\text{SnO}_2$ , respectively, while the peaks at  $2\theta = 29.2^\circ$  and  $44.8^\circ$  belong to SnO. A metallic Sn phase was also present, as confirmed by the peaks at  $30.52^\circ$ ,  $32.03^\circ$ , and  $43.8^\circ$ ; this phase was attributable to the reduction of the  $\text{Sn}^{+4}$  ions to  $\text{Sn}^{+2}$  and  $\text{Sn}^0$  by the carbon layer during the high-temperature treatment. The melting temperature of Sn is far lower than the annealing temperature. Thus, any Sn formed during annealing will be liquid and SnO may also be able to sinter and diffuse into the fiber core. These results are consistent with the standard JCPDS values (JCPDS Card Nos. 41-1445( $\text{SnO}_2$ ), 06-0395(SnO), and 04-0673(Sn)). The broad peak at  $20\text{--}25^\circ$  corresponds to the graphitic carbon produced from PAN. In this case, the peak near at  $21^\circ$  indicates the presence of low crystallinity or disordered carbon. Further, in the case of the samples with a low concentration of Sn, no peaks related to  $\text{SnO}_x$  were observed.

Fig. 2b shows the Raman spectra of the  $\text{SnO}_x/\text{CNF}$  composites. The spectra were recorded using a 532 nm laser source for wavenumbers of  $1000\text{--}2000\text{ cm}^{-1}$ . The characteristic carbon-related D

and G bands corresponding to disordering (i.e., defects) in carbon and graphitic carbon ( $\text{sp}^2$ -conjugated bonds), respectively, can be observed for all the samples. The D band is observed at  $1356$ ,  $1356$ , and  $1355\text{ cm}^{-1}$  in the case of SnO-1, SnO-2, and SnO-3, respectively, while the G band is observed at  $1586$ ,  $1589$ , and  $1590\text{ cm}^{-1}$ , respectively. The intensity ratios of the D and G bands for SnO-1, SnO-2, and SnO-3 were approximately 1.02, 1.0, and 1.12 respectively. This confirmed that the carbon in the  $\text{SnO}_x/\text{CNF}$  nanocomposites was in a relatively disordered form.

The chemical compositions of the surfaces of the  $\text{SnO}_x/\text{CNF}$  composite mats were determined through XPS. The XPS spectra contain peaks related to Sn (Sn 3p, Sn 3d, and Sn 4d) and oxygen (O 1s), which are attributable to  $\text{SnO}_x$ . The C 1s peak is attributable to the graphitization of the CNFs while the N 1s is due to nitrogen from PAN (see Fig. 2c). The high resolution N1s spectrum is presented in Fig. S1. The atomic concentration of the elements determined by XPS is C 1s—74.2%, O 1s—11.6%, N 1s—10.9% and Sn 3d—3.3%. The high-resolution Sn spectrum in Fig. 2d shows Sn  $3d_{5/2}$  and Sn  $3d_{3/2}$  peaks at 487.5 and 495.9 eV, respectively (the peak-to-peak separation is 8.4 eV). The peak-to-peak separation energy indicates that the oxidation state of Sn is 4+. However, the different phases of Sn as observed in the XRD patterns are consistent with the three subpeaks seen in the deconvoluted Sn  $3d_{5/2}$  peak. These can be assigned to the  $\text{Sn}^0$ ,  $\text{Sn}^{2+}$ , and  $\text{Sn}^{4+}$  states (see inset of Fig. 2d). These results confirmed the presence of metallic Sn, SnO, and  $\text{SnO}_2$ ; the formation of Sn was attributable to carbothermal reduction during the high-temperature calcination process.

The morphologies of the  $\text{SnO}_x/\text{CNF}$  composites were determined using scanning electron microscopy; the images of the various samples are shown in Fig. 3, each at two different magnifications. Both the surface roughness and the diameter of the fibers in the  $\text{SnO}_x/\text{CNF}$  mats increased significantly with increasing Sn content. For the sample with a SnAc concentration of 4 wt%, a few quasi-spherical, bead-like  $\text{SnO}_x$  particles can be seen embedded in the NFs. The pores in the composite fibers are also clearly visible (see the inset image in Fig. 3f (second row)). These pores are attributable to the removal of PMMA during the high-temperature carbonization process. Fig. S2 shows SEM images of the SnO-0 (only CNF) and SnO-4 ( $\text{SnO}_x/\text{CNF}$  with 6 wt% SnAc) samples.



**Fig. 2.** (a) XRD patterns of various  $\text{SnO}_x/\text{CNF}$  composite samples. (b) Raman spectra of various  $\text{SnO}_x/\text{CNF}$  samples. (c) XPS survey spectrum of  $\text{SnO}_x/\text{CNF}$  composite sample SnO-3. (d) High-resolution Sn 3d spectrum of SnO-3 (inset shows deconvoluted Sn  $3d_{5/2}$  spectrum).

Transmission electron microscopy images of sample SnO-3 are shown in Fig. 4a. The images clearly show the core-shell structure, with a core diameter of  $\sim 225$  nm and shell thickness of  $\sim 45$  nm. Fig. 4b is a high-resolution TEM image showing a cross-sectional view of a fiber, with a  $\text{SnO}_x$  core confined within a CNF shell. The annealing temperature is far above the melting temperature of Sn, nearing the melting temperature of SnO, but is far below the

melting point of  $\text{SnO}_2$ . Thus, any Sn formed during annealing will be liquid and SnO may be able to sinter and diffuse. However,  $\text{SnO}_2$  will be relatively immobile. This type of conversion to Sn and SnO may facilitate the migration of Sn to the core of the fiber. Liquid Sn has a very high surface energy, which would promote its movement to the core of the fiber. Accordingly, we observed the distribution of Sn in the core along with SnO, via HRTEM. Two sets of fringes with

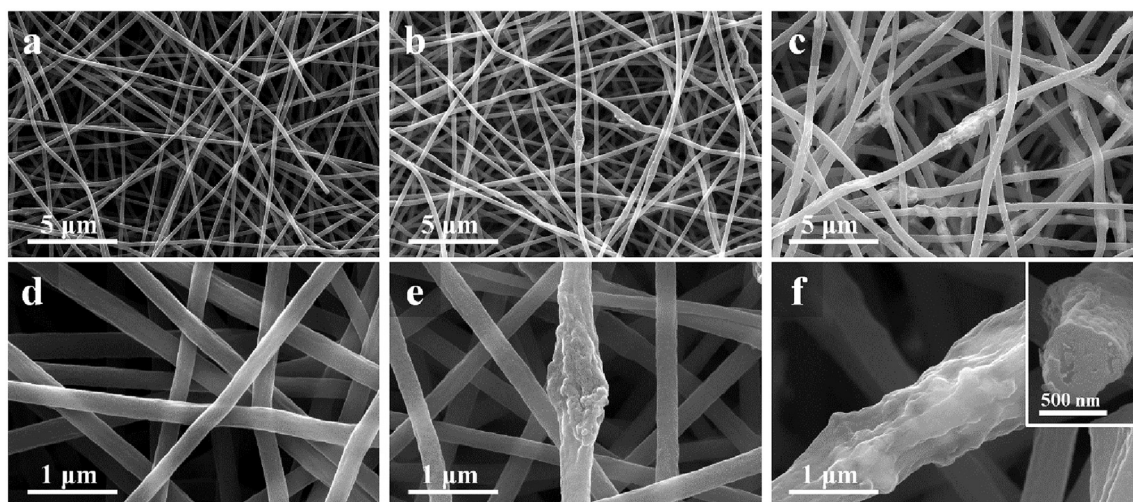


**Fig. 3.** SEM images of (a,d) SnO-1, (b,e) SnO-2, and (c,f) SnO-3. Inset in (f) is a cross-sectional view of a fiber in sample SnO-3.

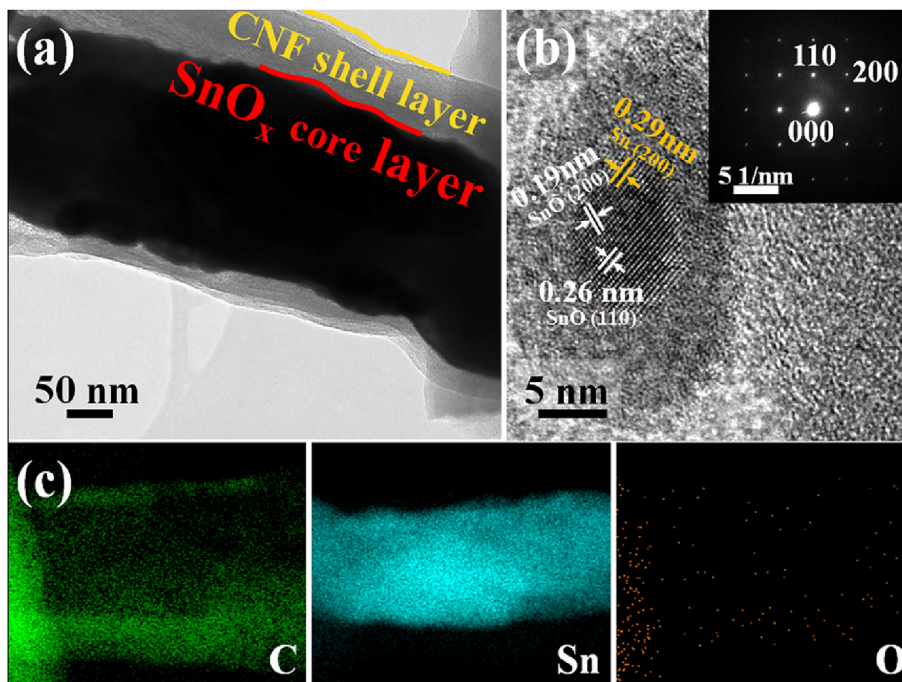


Fig. 4. (a) TEM image of SnO-3, (b) HRTEM image of SnO-3 (inset shows the corresponding SAED pattern), and (c) EDS elemental maps for C, Sn, and O.

spacing of 0.19 and 0.26 nm can be observed; these correspond to the (200) and (110) planes of SnO, respectively. In addition, lattice fringes of 0.29 nm spacing, attributed to (200) planes of Sn, are visible. The selected-area electron diffraction (SAED) pattern in the inset of Fig. 4b shows the diffraction spots of SnO, which were indexed to the (110) and (200) planes with interplanar spacing of 0.26 nm and 0.19 nm, respectively. Thus, HRTEM confirms the presence of SnO in the fiber core. The energy-dispersive X-ray spectroscopy (EDS) maps shown in Fig. 4c confirm that carbon forms a shell, covering on the core, which consists of Sn and O. The elemental mapping images in Fig. 4c shows that Sn is inside the fiber core surrounded by SnO, which is manifested with the oxygen content.

The supercapacitor potential window or range of potentials between which the physical and chemical processes corresponding to the phenomenon of pseudocapacitance occur is of critical importance. In this study, we investigated the current-voltage characteristics for a potential window ranging from  $-0.6$  V to  $0.6$  V. Fig. 5a–c shows the CV responses of symmetric supercapacitors based on samples SnO-1, SnO-2, and SnO-3. All three supercapacitors exhibited near-ideal pseudocapacitance behavior at different scan rates ( $10$ ,  $30$ ,  $50$ , and  $100$   $\text{mV} \cdot \text{s}^{-1}$ ). The CV curve for each sample was a quasi-rectangle and indicative of good charge propagation within the electrodes [30]. The quasi-rectangular shape can be attributed to the core-shell structure of the composites. The combined EDLC of CNFs and pseudo-capacitance of  $\text{SnO}_x$  is superior to the EDLC of CNFs alone. The enhanced conductivity provided by the carbon-shell material maximizes the utilization of the  $\text{SnO}_x$  pseudo-capacitance.

The decomposition of PMMA during carbonization and the presence of  $\text{SnO}_x$  improve ionic conductivity [31]. In addition, the high current observed at all the scan rates is associated with the redox reactions. The negative current observed in the current curves is due to the adsorption and/or absorption of  $\text{K}^+$  cations and the desorption of  $\text{OH}^-$  anions. On the other hand, the desorption of the cations and the absorption/adsorption of the anions owing to positive polarization is the reason for the positive current. That is to

say, the polarity of the current is primarily determined by the direction in which the voltage scan is performed. The area under the CV curves increases with an increase in the scan rate, owing to the increase in the current because of the redox reaction. The integrated area under the current curve was considered for measuring the specific capacitance along with scan rate as described in Eq. (1). Although the current and the integrated area increases with the scan rate, the specific capacitance decreases. This decrease in the specific capacitance at a high scan rate was due to the limited interaction of electrolytic ions with the electrode surface. The charge storage at the interface was less efficient at higher scan rate.

Fig. 5a–c shows that there was a significant increase in the capacitance and current outputs for the corresponding scan rates for SnO-1, SnO-2, and SnO-3. Fig. 5a–c also confirms that a case of SnO-3 is the optimal one for ensuring that the synergetic effect of the CNFs and  $\text{SnO}_x$  is strong. This synergetic effect results in maximum specific capacitances of 398, 307, 289, 245, and 221  $\text{F} \cdot \text{g}^{-1}$  in the case of the core-shell composite SnO-3 for scan rates of 2, 5, 10, 50, and 100  $\text{mV} \cdot \text{s}^{-1}$  respectively. These values highlight the good scan rate capability of sample SnO-3, with the sample exhibiting a capacitance retention (fraction of the limiting capacitance at low scan rate) of  $\sim 56\%$  at  $100$   $\text{mV} \cdot \text{s}^{-1}$ . The specific capacitance ( $C$ ) was calculated using Eq. (1) [32,33]:

$$C = \frac{4}{msV} \int_{V_-}^{V_+} i(V)dV \quad (1)$$

where  $s$  is the scan rate ( $\text{mV} \cdot \text{s}^{-1}$ ),  $V$  is the capacitive potential range (V),  $m$  is the total mass of both electrodes (g),  $i(V)$  is the voltage-dependent output current (mA), and  $V_-$  and  $V_+$  are the lower and upper voltages of the capacitive potential range.

The results of a relative scan rate analysis performed on samples SnO-0 to SnO-4 for  $10$   $\text{mV} \cdot \text{s}^{-1}$  are shown in Fig. S3, while the respective capacitances are shown in Fig. S4. The CV curves show that the magnitude of the current for positive and negative polarities increases from SnO-0 to SnO-3. However, for SnO-4, the

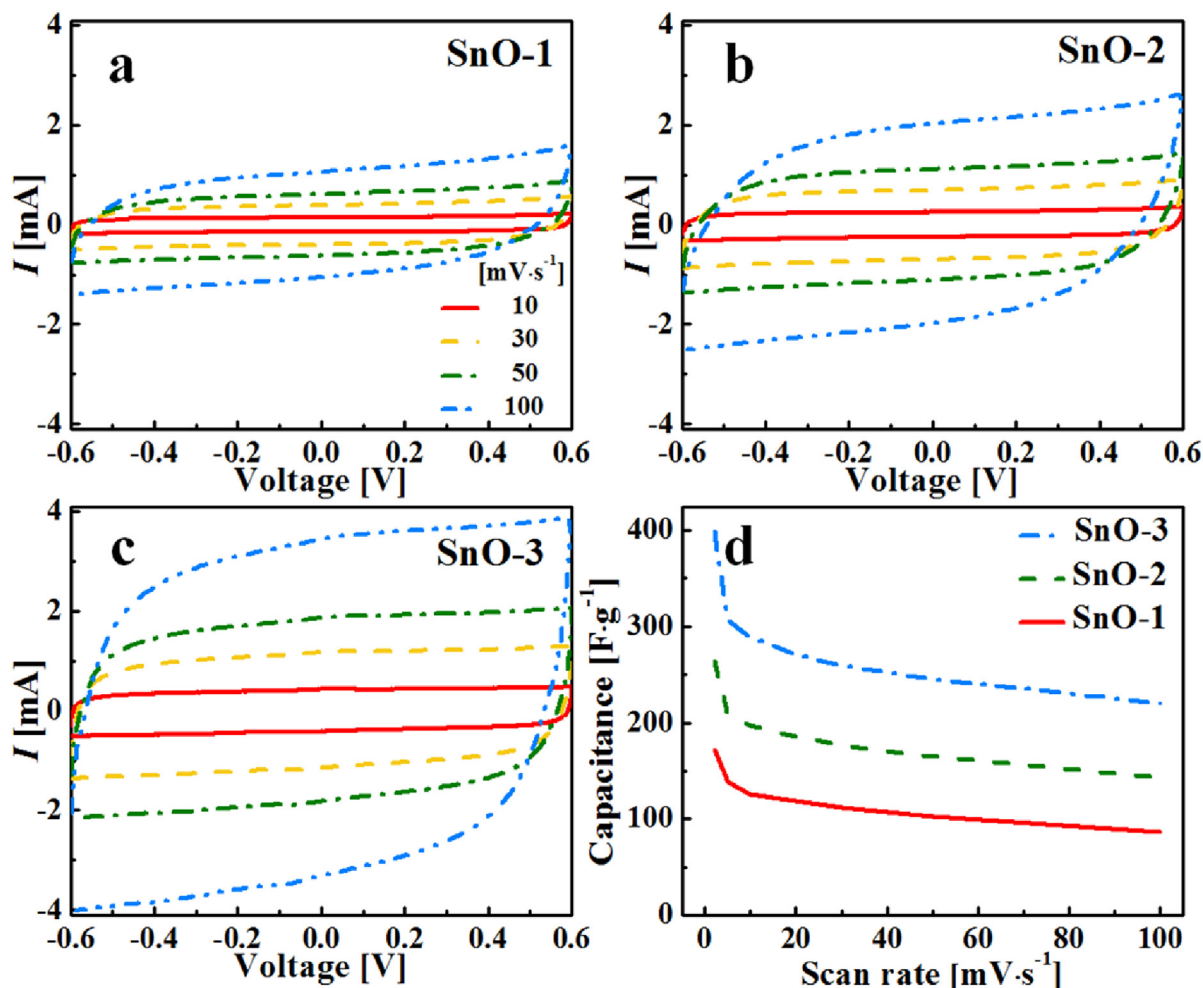


Fig. 5. CV curves for samples (a) SnO-1 (b) SnO-2, and (c) SnO-3. (d) Capacitances of  $\text{SnO}_x/\text{CNF}$  electrodes measured at different scan rates [ $\text{mV}\cdot\text{s}^{-1}$ ].

magnitude of the current is smaller than that in the case of SnO-3. Thus, the capacitance of SnO-4 was lower. This variation in the capacitance with the SnAc concentration can be understood based on Fig. S4, which shows that the capacitance increases ( $119\text{--}289 \text{ F}\cdot\text{g}^{-1}$ ) with an increase in the SnAc concentration from 0 to 4 wt%. However, for SnAc concentrations higher than 4 wt%, as in the case of SnO-4, the capacitance decreases to  $204 \text{ F}\cdot\text{g}^{-1}$ .

As shown in Fig. 5d, the capacitance decreases with increasing scan rate. This behavior is normal for electrochemical systems. Generally, two different mechanisms are involved in charge storage in oxide materials. One is the intercalation/deintercalation of protons or alkali metal cations, which leads to the complete utilization of the electrode material. This may be the reason why the specific capacitance is higher at lower scan rates. The second mechanism is related to the surface adsorption of ions at higher scan rates. Hence, only the surface of the electrode material contributes to capacity at high charge/discharge rates, which decreases the specific capacitance. At higher scan rates, the redox reaction is incomplete, due to reaction rate and ion transport limitations, but the formation of the electrostatic double-layer is not affected.

Fig. 6a shows the galvanostatic discharge curves for SnO-3 for different specific current densities ( $0.1, 0.5, 1, \text{ and } 2 \text{ A}\cdot\text{g}^{-1}$ ) in 6 M KOH as the electrolyte. The discharge curves are almost linear, exhibiting the characteristics of a supercapacitor. In addition, both the pseudocapacitance from  $\text{SnO}_x$  and EDLC from CNF enhance the specific capacitance. The discharge time decreases with increasing

current density owing to the rapid absorption/adsorption of the cations and desorption of the anions. The specific capacitance values were calculated from the discharge time using Eq. (2) [32,33]:

$$C_s = \frac{4It_d}{m(V - IR)} \quad (2)$$

where  $C_s$  is the specific capacitance ( $\text{F}\cdot\text{g}^{-1}$ ),  $t_d$  is the discharge time (s),  $I$  is the specific current (A),  $m$  is the mass of both electrodes (g),  $V$  is the capacitive potential range (V), and  $IR$  is the measure of the ohmic drop (V). In this study, we took it to be "0," as no ohmic drop was observed, as can be seen from Fig. 6a. The specific capacitance values for SnO-1, SnO-2, and SnO-3 are shown in Fig. 6b. The maximum specific capacitances for SnO-3 are  $273 \text{ and } 220 \text{ F}\cdot\text{g}^{-1}$  for specific current densities of  $0.1 \text{ and } 1 \text{ A}\cdot\text{g}^{-1}$ , respectively. The highest capacitances for SnO-1, SnO-2, and SnO-3 were calculated to be 212, 247, and  $273 \text{ F}\cdot\text{g}^{-1}$  respectively.

The long-term cycling performance is an important parameter for assessing the performance of supercapacitors and electrodes. Thus, the first and last three galvanostatic charge/discharge curves of SnO-3 corresponding to cycling for 5000 cycles at a current density of  $1 \text{ A}\cdot\text{g}^{-1}$  are shown in Fig. 6c. The near-symmetric nature of the triangular charge/discharge curves is indicative of the capacitive behavior of the supercapacitor. Similarly, scan-rate-dependent CV curves were also obtained for 5000 cycles.

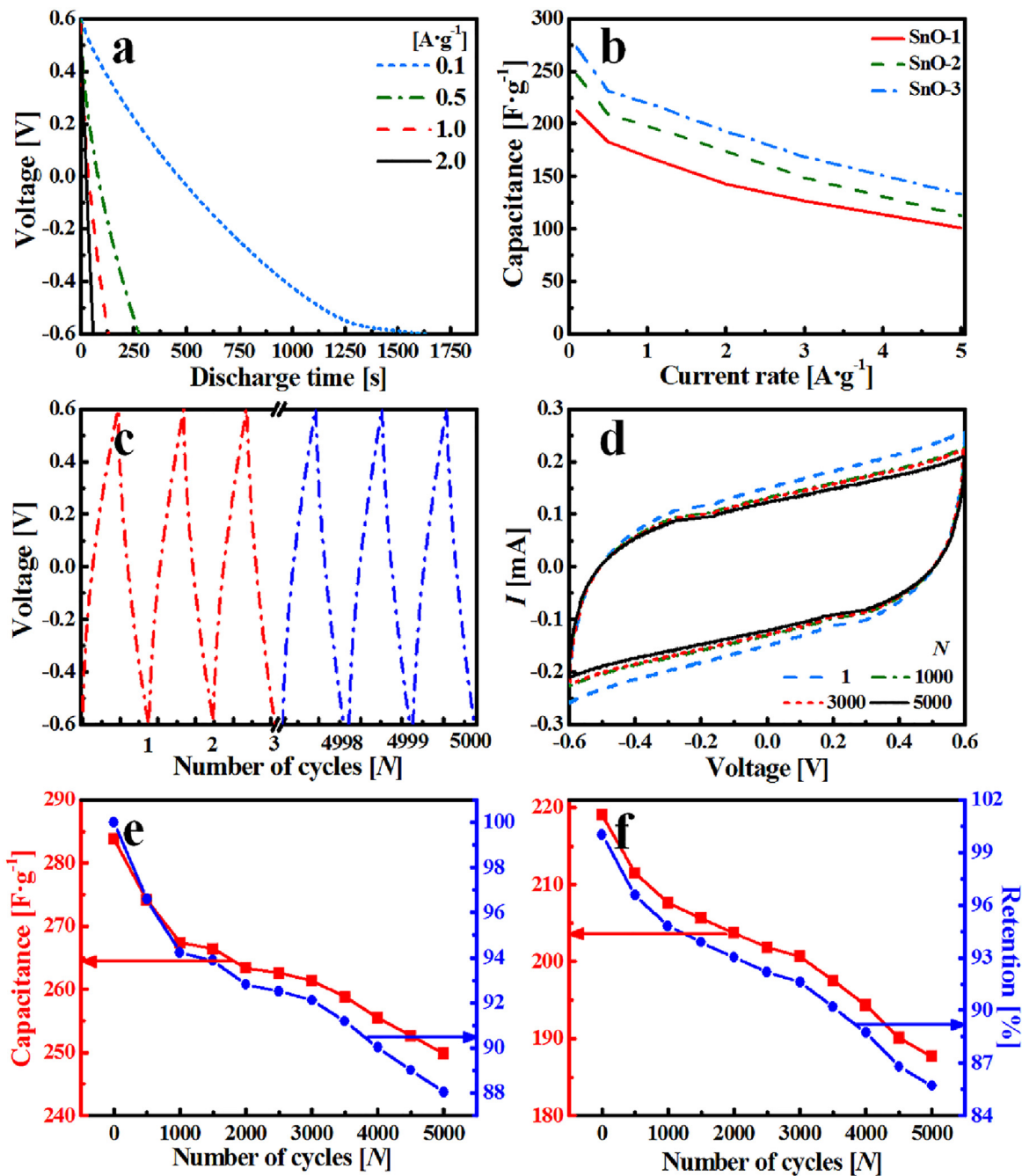


**Fig. 6.** Current-density-dependent (a) galvanostatic discharge profiles of SnO-3 for different specific current densities and (b) specific capacitances [ $\text{F}\cdot\text{g}^{-1}$ ] of various samples. (c) Long-term cycling performance of SnO-3 at  $1 \text{ A}\cdot\text{g}^{-1}$  and (d) its CV curves at a scan rate of  $10 \text{ mV}\cdot\text{s}^{-1}$ . Specific capacitance [ $\text{F}\cdot\text{g}^{-1}$ ] and capacity retention [%] of SnO-3 for over 5000 cycles (e) at a current density of  $1 \text{ A}\cdot\text{g}^{-1}$  and (f) scan rate of  $10 \text{ mV}\cdot\text{s}^{-1}$ .

Representative curves are shown in Fig. 6d. It can be seen that the curves are quasi-rectangular, with the area under the curves decreasing slightly with the increase in the scan rate. The specific capacitance as determined from the charge/discharge curves for a current density of  $1 \text{ A}\cdot\text{g}^{-1}$  varies from 217 to  $202 \text{ F}\cdot\text{g}^{-1}$  over 5000 cycles, retaining ~86% of the capacitance observed in the first cycle (see Fig. 6e). Further, Fig. 6f shows the specific capacitance and capacity retention of SnO-3 over 5000 cycles for a scan rate of  $10 \text{ mV}\cdot\text{s}^{-1}$  over the potential range of  $-0.6$  to  $0.6 \text{ V}$ . Its capacitance decreased from 283 to  $257 \text{ F}\cdot\text{g}^{-1}$  over 5000 cycles, retaining 88% of the initial capacitance. The long-term cycling stability of SnO-3 is attributable to its low charge-transfer resistance ( $R_{ct}$ ) and solution

resistance ( $R_s$ ). This was confirmed by electrochemical impedance spectroscopy, as described below. Compared to the specific capacitance values reported previously for supercapacitors based on similar materials (see Table 1), the values obtained in the present study are quite high, especially if one considers that an alkaline aqueous electrolyte was used and no current collector was required.

The electrochemical impedance spectra of SnO-0, 1, 2 and 3 are shown in Fig. 7a, over a frequency range of  $0.1$ – $10^5 \text{ Hz}$ . The Nyquist plots show the frequency response of the electrode and electrolyte in terms of the real ( $Z'$ ) and imaginary ( $Z''$ ) impedances. The Nyquist plot, which was obtained using an open-circuit potential, contains a

**Table 1**

Comparison of specific capacitances of electrodes of similar materials and those of the composites synthesized in the present study.

Materials	Method/Current collector	Capacitance [F·g <sup>-1</sup> ]	Scan rate [mV·s <sup>-1</sup> ]	Current density [mA·g <sup>-1</sup> ]	Potential window [V]	Electrolyte Ref.
SnO <sub>2</sub> /Carbon	Reactions under autogenic pressure at elevated temperature/Glassy carbon	37	5	–	0–1	1 <sup>a</sup> [43]
SnO <sub>2</sub> /graphene	–/Glassy carbon	43	1	–	0–1	1 <sup>a</sup> [30]
SnO <sub>2</sub> /CNF	Electrospinning and Hydrothermal/Ni Foam	187	20	–	–0.2–0.8	1 <sup>a</sup> [20]
SnO <sub>2</sub> /rGO	Microwave assisted/Carbon paper	348	–	50	0–1	1 <sup>a</sup> [12]
SnO <sub>2</sub> /Graphene/ PEDOT	–/Stainless steel	184	1	–	–0.5–0.5	1 <sup>a</sup> [19]
Hollow SnO <sub>2</sub>	Hydrothermal Ni Foam	178	1	–	–0.6–0.55	1 <sup>b</sup> [44]
SnO <sub>2</sub> /CC	Hydrothermal Carbon cloth	247	–	1000	–0.6–0.3	0.5 <sup>c</sup> [5]
SnO <sub>2</sub> /CNF	Electrospinning	118	–	1000	0–1	1 <sup>a</sup> [13]
SnO <sub>x</sub> /CNF	Electrospinning	289	10	–	–0.6–0.6	6 <sup>b</sup> Present
SnO <sub>x</sub> /CNF	Electrospinning	273	–	100	–0.6–0.6	6 <sup>b</sup> Present

<sup>a</sup> M H<sub>2</sub>SO<sub>4</sub>.<sup>b</sup> M KOH.<sup>c</sup> M LiNO<sub>3</sub>.

Warburg impedance region at low frequencies, indicating the rapid diffusion of the electrolyte ions and good capacitive behavior [34]. In addition, the slope corresponding to the Warburg region is higher than 45°, confirming the high surface roughness of the electrodes owing to the presence of pores [35]. Magnified views of the high-frequency region of the Nyquist plots are shown in Fig. 7b; this part of the plot can be attributed to the intrinsic resistance of the electrodes and the ionic resistance of the electrolyte. The Nyquist plots were fitted in accordance with Randle equivalent

circuit using ZSim software. The equivalent circuit is as shown in Fig. S5, where  $R_s$  is solution resistance,  $R_{ct}$  is charge transfer resistance,  $C$  is capacitance,  $W$  is Warburg impedance and CPE is constant phase element. The  $R_s$  for the SnO-0, 1, 2 and 3 (1.91, 0.58, 1.94 and 0.11  $\Omega$  respectively) are very small as demonstrated in Fig. 7a and b. Furthermore, the corresponding  $R_{ct}$  for the samples mentioned earlier are 120.4, 2.97, 3.10 and 7.82  $\Omega$  respectively. Although, SnO-0 exhibits a perfect semicircle, as shown in Fig. 7a, the  $R_{ct}$  is very large compared to that of SnO-3. The large impedance

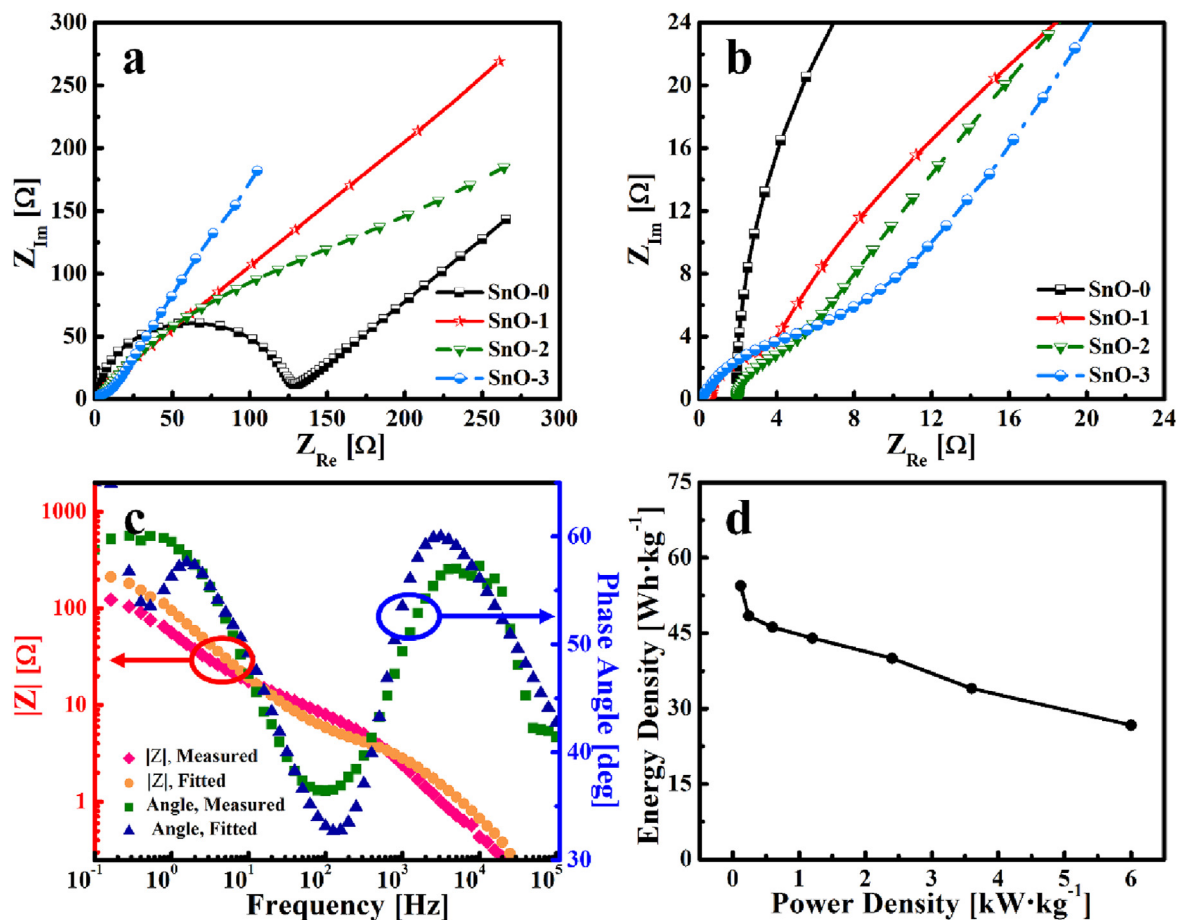


**Fig. 7.** (a) Nyquist plots for SnO-0, 1, 2 and 3 for frequencies ranging from 0.1 Hz to  $10^5$  Hz, (b) magnified version of the Nyquist plot, (c) Bode Plot of impedance modulus and phase angle and (d) plot of power and energy density of SnO-3.

of SnO-0 could be due to absence of oxide or pseudocapacitive material. The partial semicircle observed in the high-to-medium frequency region and the lower impedance ( $R_{ct}$ ) for SnO-1, SnO-2 and SnO-3 indicates better charge-transfer for the CNF composites due to decreased ion-diffusion path [21,36]. The lower  $R_{ct}$  of the composite fibers supports their improved electrochemical performance in comparison to that of SnO-0 as shown Fig. S3. The  $R_{ct}$  of SnO-1 and SnO-2 were observed to be slightly smaller than SnO-3, and this could be due to lower oxide concentration; however, the Warburg regime for SnO-3 still exhibits better diffusion characteristics. Additionally, the declined performance SnO-2 in the Warburg regime at very low frequency could have been compensated by its lower  $R_{ct}$  and due to better slope in the medium-frequency range (see Fig. 7b), which supports its better performance in comparison to SnO-0 and SnO-1 [37]. The low solution resistance and charge-transfer resistance can be attributed to the fact that the composite is binder free.

The Bode plot of SnO-3, given in Fig. 7c, shows the dependence of the electrochemical impedance modulus and phase angle on the frequency. The impedance modulus is given by  $|Z| = (Z'^2 + Z''^2)^{1/2}$ . The magnitude of the real and imaginary impedance  $|Z|$  is low at higher frequencies which is attributed to the low viscosity and high conductivity of the electrolyte [38]. The phase angle changes with the sinusoidal frequency when the instantaneous amplitude changes. The change in the phase angle reflects the impedance shift from the capacitive region (lower frequency) to the capacitive-resistive region (medium frequency), and finally to the resistive region (higher frequency). The phase angle indicates that the regions [39] corresponding to the low, medium and high frequencies are the capacitive, resistive-capacitive, and resistive regions, respectively. Fig. 7c shows that the phase angle was  $60^\circ$  at low frequencies and reflective of the contributions of the capacitance from EDLC and the pseudocapacitance from SnO<sub>x</sub>. The relaxation time constant,  $\tau_0$ , was calculated to be 80 ms for a phase angle of  $45^\circ$ . This relaxation time is considered a figure of merit for supercapacitors. Fig. 7c shows that SnO-3 exhibited pure capacitive behavior at frequencies lower than 15 Hz and that most of the energy stored in the electrodes was accessible at these frequencies. The Ragone chart of the energy and power density of SnO-3 for varying current densities ( $0.1\text{--}5\text{ A}\cdot\text{g}^{-1}$ ) is shown in Fig. 7d. The chart was plotted using the equations given by Liu et al. [40]. As can be seen from the Ragone chart, the energy density is as high as  $44\text{ Wh}\cdot\text{kg}^{-1}$  for a power density of  $1.2\text{ kW}\cdot\text{kg}^{-1}$ ; these values are higher than those for CNFs [41] as well as for a recently reported freestanding SnO<sub>2</sub>/CNF composite [13,42] and are indicative of rapid charging/discharging capability. Byun et al. [42] recently reported flexible electrodes that can be used with various electrolytes, while Ge et al. [13] reported electrodes that can be bent readily. However, in comparison to these electrodes, the ones fabricated in the present study exhibited higher capacities as well as higher energy and power densities.

#### 4. Conclusions

Free-standing flexible core-shell SnO<sub>x</sub>/CNF composite mats were fabricated by a single-nozzle electrospinning process followed by annealing. The high electrical conductivity of the CNF component allowed these to be used without a current collector. The composite nanofiber electrodes were tested in supercapacitors, and the SnO<sub>x</sub> content of the fibers was optimized to achieve the specific capacitance of up to  $289\text{ F}\cdot\text{g}^{-1}$  at a scan rate of  $10\text{ mV}\cdot\text{s}^{-1}$ . The supercapacitors maintained high specific capacitances after cycling, retaining ~86% of their initial capacitance after 5000 cycles at a current density of  $1\text{ A}\cdot\text{g}^{-1}$ . This exceptional stability during long-term cycling is attributable to the core-shell structure of the

nanofibers, as well as the synergistic effect of the conductive CNFs and electrochemically active SnO<sub>x</sub>. The ability to produce high-performance supercapacitor electrode materials by such a simple process may lead to enhanced commercial opportunities for supercapacitors across a wide range of applications where high power density is required.

#### Acknowledgement

This research was supported by Global Frontier Program through the Global Frontier Hybrid Interface Materials (GFHIM) of the National Research Foundation of Korea (NRF) funded by the Ministry of Science, ICT & Future Planning (2013M3A6B1078879), and NRF-2016M1A2A2936760, and NRF-2017R1A2B4005639.

#### Appendix A. Supplementary data

Supplementary data related to this article can be found at <http://dx.doi.org/10.1016/j.jallcom.2017.09.103>.

#### References

- [1] G.Z. Chen, Supercapacitor and supercapattery as emerging electrochemical energy stores, *Int. Mater. Rev.* 62 (2017) 173–202.
- [2] L. Guan, L. Yu, G.Z. Chen, Capacitive and non-capacitive faradaic charge storage, *Electrochim. Acta* 206 (2016) 464–478.
- [3] Y. Tan, Muhammad Asif, Lujun Pan, Jiayan Li, Muhammad Rashad, Xin Fu, Ruixue Cui, Muhammad Usman, Improved performance of a MnO<sub>2</sub>/PANI nanocomposite synthesized on 3D graphene as a binder free electrode for supercapacitors, *RSC Adv.* 6 (2016) 46100–46107.
- [4] Jeliza S. Bonso, John P. Ferraris, Nimali C. Abeykoon, Supercapacitor performance of carbon nanofiber electrodes derived from immiscible PAN/PMMA polymer blends, *RSC Adv.* 5 (2015) 19865–19873.
- [5] Z. Hu, Yadi Zhang, Yarong Liang, Yuying Yang, Ning An, Zhimin Li, Hongying Wu, Growth of 3D SnO<sub>2</sub> nanosheets on carbon cloth as a binder-free electrode for supercapacitors, *J. Mater. Chem. A* 3 (2015) 15057–15067.
- [6] Q. Ke, J. Wang, Graphene-based materials for supercapacitor electrodes – a review, *J. Mater. Chem.* 2 (2016) 37–54.
- [7] D. Xiang, L. Yin, C. Wang, L. Zhang, High electrochemical performance of RuO<sub>2</sub>-Fe<sub>2</sub>O<sub>3</sub> nanoparticles embedded ordered mesoporous carbon as a supercapacitor electrode material, *Energy* 106 (2016) 103–111.
- [8] Q. Wang, Y. Zou, C. Xiang, H. Chu, H. Zhang, F. Xu, L. Sun, C. Tang, High-performance supercapacitor based on V<sub>2</sub>O<sub>5</sub>/carbon nanotubes-super activated carbon ternary composite, *Ceram. Int.* 42 (2016) 12129–12135.
- [9] X. Li, R. Ding, W. Shi, Q. Xu, L. Wang, H. Jiang, Z. Yang, E. Liu, Hierarchical mesoporous Ni-P@MnO<sub>2</sub> composite for high performance supercapacitors, *Mater. Lett.* 187 (2017) 144–147.
- [10] M. Asif, Y. Tan, L. Pan, M. Rashad, J. Li, X. Fu, R. Cui, Synthesis of a highly efficient 3D graphene-CNT-MnO<sub>2</sub>-PANI nanocomposite as a binder free electrode material for supercapacitors, *Phys. Chem. Chem. Phys.* PCCP 18 (2016) 26854–26864.
- [11] L. Fang, B. Zhang, W. Li, J. Zhang, K. Huang, Q. Zhang, Fabrication of highly dispersed ZnO nanoparticles embedded in graphene nanosheets for high performance supercapacitors, *Electrochim. Acta* 148 (2014) 164–169.
- [12] C.-T. Hsieh, W.-Y. Lee, C.-E. Lee, H. Teng, Electrochemical capacitors fabricated with tin oxide/graphene oxide nanocomposites, *J. Phys. Chem. C* 118 (2014) 15146–15153.
- [13] Y. Qu, Jianlong Ge, Leitao Cao, Fei Wang, Lvye Dou, Jianyong Yua, Bin Ding, Polybenzoxazine-based highly porous carbon nanofibrous membranes hybridized by tin oxide nanoclusters: durable mechanical elasticity and capacitive performance, *J. Mater. Chem. A* 4 (2016) 7795–7804.
- [14] S.S. Raut, G.P. Patil, P.G. Chavan, B.R. Sankapal, Vertically aligned TiO<sub>2</sub> nanotubes: highly stable electrochemical supercapacitor, *J. Electroanal. Chem.* 780 (2016) 197–200.
- [15] Y. Zou, I.A. Kinloch, R.A. Dryfe, Mesoporous vertical Co<sub>3</sub>O<sub>4</sub> nanosheet arrays on nitrogen-doped graphene foam with enhanced charge-storage performance, *ACS Appl. Mater. Interfaces* 7 (2015) 22831–22838.
- [16] B.E. Conway, Transition from “Supercapacitor” to “Battery” behavior in electrochemical energy storage, *J. Electrochem. Soc.* 138 (1991) 1536–1548.
- [17] A. Singh, A. Chandra, Enhancing specific energy and power in asymmetric supercapacitors – a synergistic strategy based on the use of redox additive electrolytes, *Sci. Rep.* 6 (2016) 25793.
- [18] W. Xiao, H. Xia, J.Y.H. Fuh, L. Lu, Growth of single-crystal  $\alpha$ -MnO<sub>2</sub> nanotubes prepared by a hydrothermal route and their electrochemical properties, *J. Power Sources* 193 (2009) 935–938.
- [19] W. Wang, W. Lei, T. Yao, X. Xia, W. Huang, Q. Hao, X. Wang, One-pot synthesis of graphene/SnO<sub>2</sub>/PEDOT ternary electrode material for supercapacitors, *Electrochim. Acta* 108 (2013) 118–126.

- [20] J. Mu, B. Chen, Z. Guo, M. Zhang, Z. Zhang, C. Shao, Y. Liu, Tin oxide (SnO<sub>2</sub>) nanoparticles/electrospun carbon nanofibers (CNFs) heterostructures: controlled fabrication and high capacitive behavior, *J. Colloid Interface Sci.* 356 (2011) 706–712.
- [21] S. Hao, Y. Sun, Y. Liu, Y. Zhang, G. Hu, Facile synthesis of porous SnO<sub>2</sub> film grown on Ni foam applied for high-performance supercapacitors, *J. Alloys Compd.* 689 (2016) 587–592.
- [22] M. Zhi, C. Xiang, J. Li, M. Li, N. Wu, Nanostructured carbon-metal oxide composite electrodes for supercapacitors: a review, *Nanoscale* 5 (2013) 72–88.
- [23] B.N. Joshi, S. An, H.S. Jo, K.Y. Song, H.G. Park, S. Hwang, S.S. Al-Deyab, W.Y. Yoon, S.S. Yoon, Flexible, freestanding, and binder-free SnO<sub>x</sub>-ZnO/carbon nanofiber composites for lithium ion battery anodes, *ACS Appl. Mater. Interfaces* 8 (2016) 9446–9453.
- [24] C.-L. Lee, Ji-Won Jung, Sunmoon Yu, Il-Doo Kim, Electrospun nanofibers as a platform for advanced secondary batteries: a comprehensive review, *J. Mater. Chem. A* 4 (2016) 703–750.
- [25] S. Peng, L. Li, J. Kong Yoong Lee, L. Tian, M. Srinivasan, S. Adams, S. Ramakrishna, Electrospun carbon nanofibers and their hybrid composites as advanced materials for energy conversion and storage, *Nano Energy* 22 (2016) 361–395.
- [26] X. Bai, Q. Liu, J. Liu, H. Zhang, Z. Li, X. Jing, P. Liu, J. Wang, R. Li, Hierarchical Co<sub>3</sub>O<sub>4</sub>@Ni(OH)<sub>2</sub> core-shell nanosheet arrays for isolated all-solid state supercapacitor electrodes with superior electrochemical performance, *Chem. Eng. J.* 315 (2017) 35–45.
- [27] H. Chen, X.Q. Qi, M. Kuang, F. Dong, Y.X. Zhang, Hierarchical copper/nickel-based manganese dioxide core-shell nanostructure for supercapacitor electrodes, *Electrochim. Acta* 212 (2016) 671–677.
- [28] C. Kim, Y.I. Jeong, B.T. Ngoc, K.S. Yang, M. Kojima, Y.A. Kim, M. Endo, J.W. Lee, Synthesis and characterization of porous carbon nanofibers with hollow cores through the thermal treatment of electrospun copolymeric nanofiber webs, *Small* 3 (2007) 91–95.
- [29] A.L.Y. Alexander, V. Bazilevsky, Constantine M. Megaridis, Co-electrospinning of core-shell fibers using a single-nozzle technique, *Langmuir ACS J. Surf. Colloids* 23 (2007) 2311–2314.
- [30] F. Li, J. Song, H. Yang, S. Gan, Q. Zhang, D. Han, A. Ivaska, L. Niu, One-step synthesis of graphene/SnO<sub>2</sub> nanocomposites and its application in electrochemical supercapacitors, *Nanotechnology* 20 (2009) 455602.
- [31] X.L. Wu, J. Lin, J.Y. Wang, H. Guo, Electrospun PVDF/PMMA/SiO<sub>2</sub> membrane separators for rechargeable lithium-ion batteries, *Key Eng. Mater.* 645–646 (2015) 1201–1206.
- [32] L. Fan, L. Yang, X. Ni, J. Han, R. Guo, C. Zhang, Nitrogen-enriched meso-macroporous carbon fiber network as a binder-free flexible electrode for supercapacitors, *Carbon* 107 (2016) 629–637.
- [33] M.D. Stoller, R.S. Ruoff, Best practice methods for determining an electrode material's performance for ultracapacitors, *Energy Environ. Sci.* 3 (2010) 1294–1301.
- [34] D. Sun, X. Yan, J. Lang, Q. Xue, High performance supercapacitor electrode based on graphene paper via flame-induced reduction of graphene oxide paper, *J. Power Sources* 222 (2013) 52–58.
- [35] A. Sharifi-Viand, M.G. Mahjani, M. Jafarian, Investigation of anomalous diffusion and multifractal dimensions in polypyrrole film, *J. Electroanal. Chem.* 671 (2012) 51–57.
- [36] F. Ran, K. Shen, Y. Tan, B. Peng, S. Chen, W. Zhang, X. Niu, L. Kong, L. Kang, Activated hierarchical porous carbon as electrode membrane accommodated with triblock copolymer for supercapacitors, *J. Membr. Sci.* 514 (2016) 366–375.
- [37] Z. Hu, Yadi Zhang, Yarong Liang, Yuying Yang, Ning An, Zhimin Li, Hongying Wu, Growth of 3D SnO<sub>2</sub> nanosheets on carbon cloth as a binder-free electrode for supercapacitors, *J. Mater. Chem. A* 3 (2015) 15057–15067.
- [38] X. Sun, X. Zhang, H. Zhang, B. Huang, Y. Ma, Application of a novel binder for activated carbon-based electrical double layer capacitors with nonaqueous electrolytes, *J. Solid State Electrochem.* 17 (2013) 2035–2042.
- [39] S.K. Jana, B. Saha, B. Satpati, S. Banerjee, Structural and electrochemical analysis of a novel co-electrodeposited Mn<sub>2</sub>O<sub>3</sub>-Au nanocomposite thin film, *Dalton Trans.* 44 (2015) 9158–9169.
- [40] Y. Liu, J. Zhou, L. Chen, P. Zhang, W. Fu, H. Zhao, Y. Ma, X. Pan, Z. Zhang, W. Han, E. Xie, Highly flexible freestanding porous carbon nanofibers for electrode materials of high-performance all-carbon supercapacitors, *ACS Appl. Mater. Interfaces* 7 (2015) 23515–23520.
- [41] L. Zhao, Y. Qiu, J. Yu, X. Deng, C. Dai, X. Bai, Carbon nanofibers with radially grown graphene sheets derived from electrospinning for aqueous supercapacitors with high working voltage and energy density, *Nanoscale* 5 (2013) 4902–4909.
- [42] S. Byun, B. Shin, Densely packed hybrid films comprising SnO<sub>2</sub> and reduced graphite oxide for high-density electrochemical capacitors, *J. Mater. Chem. A* 4 (2016) 16175–16183.
- [43] I. Perelshtein, Ramakrishnan Kalai Selvan, Nina Perkas, Aharon Gedanken, Synthesis of hexagonal-shaped SnO<sub>2</sub> nanocrystals and SnO<sub>2</sub>@c nanocomposites for electrochemical redox supercapacitors, *J. Phys. Chem. C* 112 (2008) 1795–1802.
- [44] Y. Yang, S. Ren, S. Ma, C. Hao, M. Ji, Hollow tin dioxide microspheres with multilayered nanocrystalline shells for pseudocapacitor, *Electrochim. Acta* 155 (2015) 437–446.